AGU PUBLICATIONS

Geophysical Research Letters

RESEARCH LETTER
10.1002/2016GL071491

Key Points:
- Supercooling by pressure relief of ice shelf water results in thick accumulations of ice crystals beneath ice shelves and adjacent sea ice
- Physical characteristics of the crystal layers give rise to multiple modes of stress at the ice-ocean interface
- The resulting drag can be up to 2 orders of magnitude greater than is presently used in numerical models of ice shelf cavities

Correspondence to:
N. J. Robinson,
natalie.robinson@niwa.co.nz

Citation:
Robinson, N. J., C. L. Stevens, and M. G. McPhee (2017), Observations of amplified roughness from crystal accretion in the sub-ice ocean boundary layer, *Geophys. Res. Lett.*, *44*, 1814–1822, doi:10.1002/2016GL071491.

Received 5 OCT 2016
Accepted 4 FEB 2017
Accepted article online 7 FEB 2017
Published online 18 FEB 2017

Observations of amplified roughness from crystal accretion in the sub-ice ocean boundary layer

N. J. Robinson[1], C. L. Stevens[1,2], and M. G. McPhee[3]

[1]Marine Physics, National Institute of Water and Atmospheric Research, Wellington, New Zealand, [2]Physics Department, University of Auckland, Auckland, New Zealand, [3]McPhee Research, Naches, Washington, USA

Abstract Ice crystal accretion on the underside of sea ice and ice shelves, a signature of pressure-induced supercooling, has the potential to alter the energy balance in the ocean boundary layer through enhanced hydrodynamic roughness. Here we present estimates of crystal-driven ocean boundary layer roughness in supercooled water beneath sea ice adjacent to the McMurdo/Ross Ice Shelf. Data were collected from four sites in McMurdo Sound, Antarctica, between 2007 and 2015, and represent a range of ice shelf-affected conditions. The results show that drag of the rough ice underside in the presence of platelets is 6–30 times larger than typical levels homogeneously applied in ice-ocean interaction models. The crystal-enhanced drag promotes increased entrainment into the boundary layer from the upper ocean, which has the potential to affect ice shelf evolution and sea ice growth through enhanced turbulent exchange of heat and momentum.

Plain Language Summary Water that includes a component of meltwater can become colder than its freezing point as it ascends the ice shelf base. This can promote the growth of thick layers of ice crystals between the ice and ocean. Owing to a lack of observational evidence, computational models presently make no allowance for this granular type of interface and therefore suppress vertical mixing that may be significant for ice shelf longevity. Over five Antarctic field campaigns, we have made measurements in the ocean beneath sea ice that demonstrate the effect of thin and thick layers of ice crystals beneath the ice. We have found that there may be as much as 5 times greater water exchange near the base of the ice than when the crystals are not present. Depending on the temperature of that water, this effect could lead to either enhanced melt or freeze.

1. Introduction

Approximately 50% by area of the Antarctic ice sheet will move through cold cavity ice shelves during its descent to the ocean [*Rignot et al.*, 2013]. The three largest cold-cavity ice shelves (Filchner-Ronne, Ross & Amery) comprise 65% of the total ice shelf area but only 18% of total meltwater contribution [*Rignot et al.*, 2013]. Hence, understanding the ice-ocean interactions of cold-cavity systems is critical for predicting the rate at which land-based ice is drained and made available for sea-level contribution.

Within the cold cavities, the combination of pressure due to ice thickness and heat content in the water column stimulates production of ice shelf water (ISW) via basal melting. By definition, ISW is colder than the surface freezing point and therefore has the potential to become "supercooled" via pressure relief. This occurs as the ISW buoyantly ascends the ice shelf base and traverses the in situ salinity- and pressure-dependent freezing temperature. Refreezing of supercooled water onto the base of the ice shelf creates "Marine ice," which takes the form of layers, tens to hundreds of meters thick, of individual ice crystals that can stretch in unbroken lines from the grounding line to the calving front [*Craven et al.*, 2009; *Holland et al.*, 2009].

Beyond the ice shelf front, platelet crystals, typically 10–200 mm across [*Smith et al.*, 2001], can accumulate beneath adjacent sea ice [*Hunkeler et al.*, 2015; *Langhorne et al.*, 2015]—a spatial extension of marine ice accretion—to form layers from a few centimeters to several meters thick. The presence of platelets ice, either freely floating or consolidated into the sea ice cover, is incontrovertible evidence of direct ice shelf influence in the form of ISW that has been supercooled during its recent ascent of the ice shelf base [*Smith et al.*, 2001; *Robinson et al.*, 2014]. Different scales of time and pressure in the sub-sea ice and sub-ice shelf regimes will likely lead to differing degrees of compaction and consolidation of the layers. However, the unconsolidated and porous layer of ice crystals in direct contact and exchange with the ocean is likely to similarly affect stress transfer in the ocean boundary layer beneath both sea ice and ice shelves. In both regimes, the presence of growing ice crystals creates a physically (i.e., hydraulically) rough and thermodynamically active interface

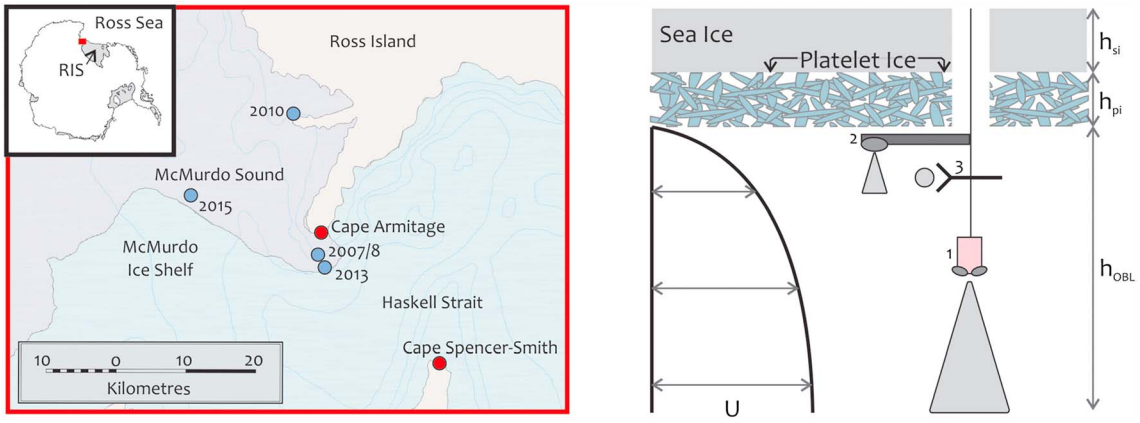

Figure 1. (left) Map of the study region with the four field sites identified by the years in which they were occupied. The red box on the inset map identifies McMurdo Sound's location at the northwestern corner of the Ross Ice Shelf. (right) Under-ice boundary-layer velocity (U) which varies with depth beneath the platelet crystals accreted on the underside of the sea ice. Also shown is a composite representation of the sensor arrangement for different campaigns: (1) 300 kHz ADCP, (2) 2 MHz ADCP, and (3) 5 MHz ADV.

with the potential to enhance turbulent exchanges via both buoyancy-induced convection [*Robinson et al.*, 2014] and shear (this study).

Due to difficulties of gaining access, the critical and complex exchanges of heat, salt, and momentum in areas of marine ice accretion are yet to be directly observed in situ. In the absence of observational evidence from supercooled boundary flows, stress transfer, represented in numerical models by a dimensionless drag coefficient C_d, is presently based on direct observations beneath smooth, melting Arctic sea ice [*Mellor et al.*, 1986; *Shirasawa and Ingram*, 1991], or in a basal melt zone [*Jenkins et al.*, 2010], with $0.0015 \leq C_d \leq 0.01$, but typically around 0.003 [e.g., *Gwyther et al.*, 2015]. This assumes a linear, uniform, static interface characterized by low surface roughness and makes no allowance for the granular nature of the interface that exists in the presence of marine ice. *Gwyther et al.* [2015] remark that C_d is the least observationally constrained parameter in the commonly used three-equation melting scheme [*Jenkins et al.*, 2010] and is often exploited as a tuning parameter.

Here we exploit the landfast sea ice of McMurdo Sound as a temporary extension of the McMurdo/Ross Ice Shelf to gain ready and repeated access to the crystal-affected ocean boundary layer. We quantify drag effects beneath platelet-affected sea ice under varying conditions from five Antarctic field campaigns. Drag was estimated at up to 2 orders of magnitude greater than is currently employed in ice shelf cavity models. It was found to be significantly greater than could be explained by either skin friction (i.e., individual crystals protruding into the ocean boundary layer) or form drag (i.e., the overall morphology of the platelet layer) contributions to hydraulic roughness, prompting two further suggested mechanisms for enhanced effective roughness. In the dynamic and vulnerable areas where the ice-shelf ocean interface is characterized by thick accumulations of marine ice, we suggest that the effect of crystal-induced drag could be even greater.

2. Methods

Boundary layer observations were recorded beneath the fast sea ice of McMurdo Sound, Antarctica, during five spring/summer field campaigns (Figure 1). The region is known to be affected by export from the nearby oceanic cavity of the Ross Ice Shelf [*Smith et al.*, 2001; *Mahoney et al.*, 2011; *Hughes et al.*, 2014; *Langhorne et al.*, 2015], and conditions encountered represent a range of supercooled water and platelet layer states. The camps all included a containerized laboratory over a 50–80 cm diameter "hydro hole" and a nearby oceanographic mooring.

Friction effects in boundary layers can be characterized as a friction velocity, $u_* = \sqrt{T_0/\rho_0}$, where T_0 is the boundary shear stress and ρ_0 is a reference density. The assumption that the velocity in the boundary layer scales with this friction results in the logarithmic law of the wall, so that $U(z) = \frac{u_*}{\kappa} \ln\left(\frac{z}{z_0}\right)$; where κ is von Karman's constant ($\kappa \cong 0.4$) and the so-called roughness length scale, z_0, is the distance length scale

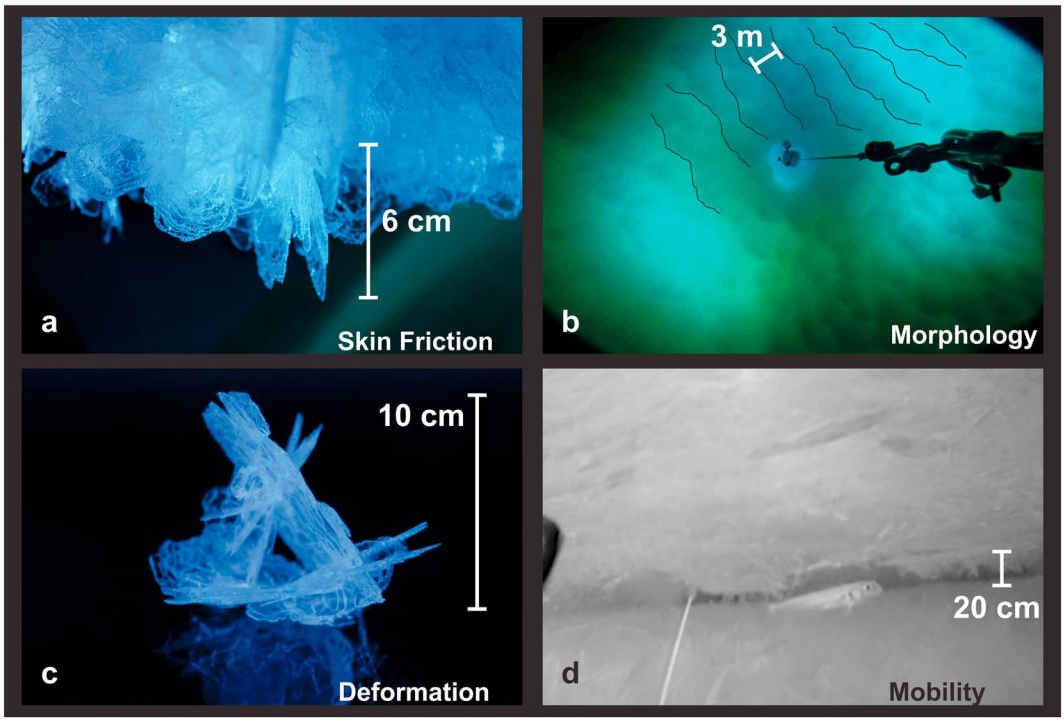

Figure 2. The various potential contributions to overall effective roughness of the boundary. (a) The interface is composed of individual ice crystals protruding into the ocean boundary layer at random orientations; (b) looking up at the base of the platelet layer from beneath, aligned ripples can be seen (example troughs identified by sketched black lines), each approximately 30 cm in height, created by buoyant sedimentation of ice crystals; (c) platelet ice crystals grow through one another to create an open structure, which may deform or collapse in response to stress; (d) where background flows are sufficiently high, the coherent platelet structure may become disassociated from the solid sea ice above, able to move independently in response to circulation of the upper ocean.

associated with the level of zero flow—not to be directly compared with physical size of roughness elements. Separating out terms, the law of the wall becomes

$$U(z) = \frac{u_*}{\kappa}\ln(z) - \frac{u_*}{\kappa}\ln(z_0) = a\ln(z) + b$$

which allows independent estimation of u_* from the slope and z_0 from the zero-crossing of the boundary layer logarithmic profile. Models typically reduce this boundary layer representation to a drag coefficient C_d, where $u_*^2 = C_d u_\infty^2$, in which u_∞ is the far-field velocity, representative of current speed in the ocean interior.

As formulated, the drag coefficient is invariant of background flow speed. However, for background flows less than 0.05 m s^{-1}, and consequently with small boundary stress, the planetary vertical scale associated with the Earth's rotation can be smaller than the geometric (physical) scale at which sampling takes place. Therefore, since measured estimates of boundary layer structure may be ill defined beneath this threshold value of 0.05 m s^{-1} [*McPhee*, 2008, section 5.1.2], these estimates have been identified in the present analysis.

As the field campaigns evolved, so too did the instrumentation resulting in three different velocity acquisition methods across the five campaigns. While not ideal, the methods all appeal to the same well-established law of the wall model for estimating C_d.

December 2007. The camp was located on multiyear sea ice at the northern edge of the McMurdo Ice Shelf, underlain by ~1.5 m of platelet layer (Figure 2a). An RD Instruments 307.2 Hz Workhorse acoustic Doppler current profiler (ADCP) was suspended 2 m beneath the platelet-ocean interface looking down. Instantaneous velocity profiles, in 2 m bins to a nominal depth of 112 m, were collected every 6 s and output as average profiles every 5 min. C_d was estimated from sequential 20 min mean profiles from the slope of the logarithmic fit over the top 20 m of each profile, i.e., $C_d = u_*^2/u_\infty^2$, where u_∞^2 is taken as the mean current speed at 60 m. This length of data segment was sufficiently short that the boundary layer structure should not change significantly in this time, but long enough to provide a meaningful profile. A SeaBird Electronics SBE 19 plus

conductivity-temperature-depth sampling at 4 Hz was also used to collect full-depth profiles of temperature and salinity.

September 2008. The location and experiment setup was identical to that used in 2007, except that no platelet ice was observed despite the water column being supercooled to 30 m depth. The lack of platelet ice is likely due to occupying the site 2 months earlier in the season which, due to seasonal variation in regional circulation patterns, meant that the site was deprived of ISW influence, and hence platelet ice, until late spring/early summer [e.g., *Mahoney et al*., 2011].

October to November 2010. This field camp was the least affected by ice shelf water. Nevertheless, supercooled water and platelet ice were present, albeit in a thin layer. A single-point ADV (Acoustic Doppler Velocimeter, Sontek) measured turbulent fluctuations, and C_d was determined from $u_* = \left(\langle u'w' \rangle^2 + \langle v'w' \rangle^2\right)^{1/4}$ [*McPhee et al*., 2016].

October to November 2013 and 2015. The velocity structure was captured using a 2 MHz Nortek Aquadopp acoustic Doppler profiler (HR-Adopp). This was mounted on a folding arm which allowed the instrument to be positioned flush with the underside of the platelet layer. The HR-Adopp sampled with 0.01 m bins, at 1 s intervals, over 1 m with a blanking distance of 10 cm. Data were continuously acquired and then, for the present analysis, divided into 10 min sections. This data segment duration was chosen as a compromise between the averaging improving the quality of the result versus the reduction in capturing the variability in flow [*Friedrichs and Wright*, 1997]. The logarithmic boundary layer model was then fitted to each average profile to obtain an estimate of C_d.

3. Results

3.1. Physical Characteristics of the Platelet Layer

Visual inspection of the underside of the platelets (Figure 2a) revealed that the physical roughness was very different to that of sea ice formed away from ice shelf influence, or in its melting phase. Thick accumulations of platelet crystals formed structured and porous lattices as they continued to grow through each other, having floated to the interface in random orientations (Figure 2c). In 2013 and 2015, this was apparent after a hot water jet had been used to remove ~80 × 80 cm blocks of solid sea ice. This exposed a semiconsolidated layer of platelet crystals spanning the base of the hole that stayed in place, rather than collapsing upwards—i.e., its internal structure was sufficiently strong that it withstood its own buoyancy. When viewed from below (Figure 2b), the platelet crystals had deposited to form aligned ripples, each ~30 cm tall and spaced 2–3 m apart. It is not known whether these were an expression of the basal topography of the sea ice or whether they evolved from buoyant sedimentation of ice crystals in a manner analogous to dune formation by sedimentation of grains.

In 2007, on repeat visits to the site, it was apparent that a new section of platelet layer had moved into place beneath the stationery hole in the sea ice, as the hole through the platelet lattice had to be remade by punching through it with a ballast block. This implied that the platelet layer was separated from the base of the sea ice, and able to move with the ocean currents, which were significantly faster at this site than at the other field camps. Using underwater camera equipment with a live feed, this separation was confirmed with the observation of a 20 cm gap between the sea ice and platelet ice layer (Figure 2d).

3.2. Velocity Structure of the Ocean Boundary Layer

Profiles of current speed collected in 2007 and 2008 (Figure 3) reveal the very different response of the ocean boundary layer to the presence or absence of a thick and mobile layer of platelet crystals. In the absence of any platelets (2008, Figure 3a) shear induced by the boundary was insufficient to register any effect on the boundary layer profile. This does not imply that law-of-the-wall behavior was absent but that it was of insufficient vertical scale to be captured in the observations.

In stark contrast, a reduction in current speed over the upper ~30 m was apparent (Figure 3b) in the platelet-affected boundary layer. The density structure at this time (Figure 3b) revealed a neutrally buoyant layer to ~50 m and demonstrated that the modified velocity profile was not dependent on stratification. The logarithmic structure clustered around peaks in tidal flow, taken to represent a "stable" mode. The velocity structure during tidal troughs (Figure 3c) was very different and may represent a "transitional" phase or "unstable" mode associated with the platelet layer's response to rapidly changing ocean current direction.

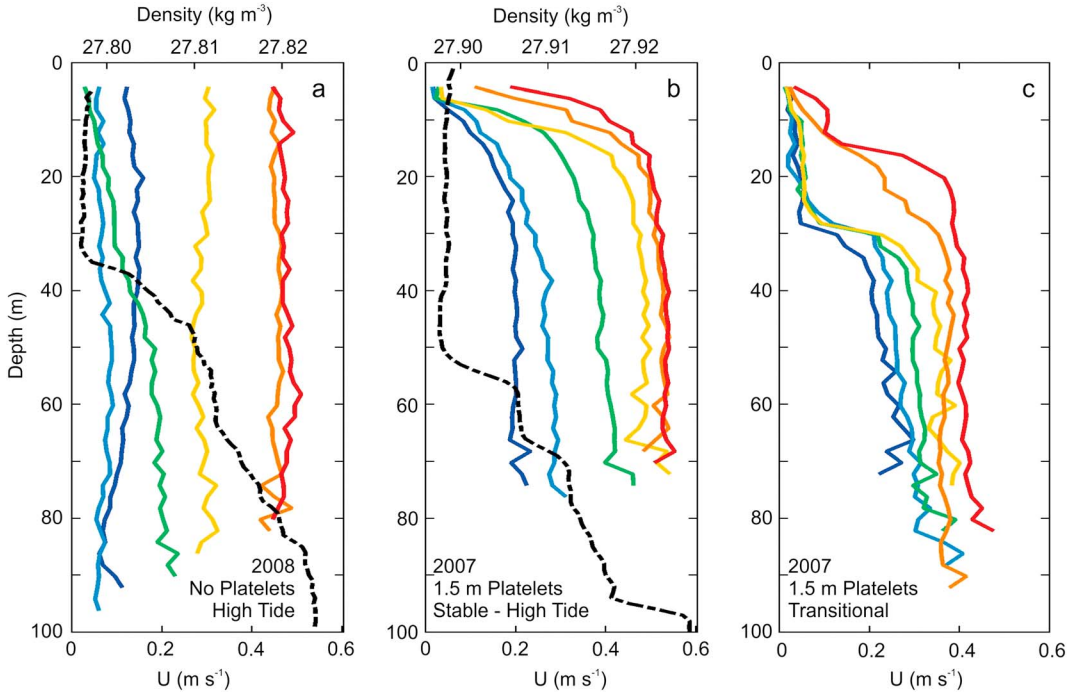

Figure 3. Speed profiles in the upper ocean under different platelet conditions (hourly progression from dark blue to red) with synchronous density profiles (black dashed lines) as available. (a) Six hours preceding and including, peak high tide, September 2008, when no platelet ice crystals were observed beneath the sea ice; (b) Six hours preceding and including peak high tide, December 2007, when a 1.5 m thick platelet layer was observed beneath, and able to move independently of, the sea ice; (c) Six hours over flood tide, December 2007, when the same 1.5 m thick platelet layer was subject to a rapid and dramatic change in background flow direction.

3.3. Synthesis of C_d Estimates

The stress transfer is explored here via a synthesis of drag coefficient estimates from all four platelet-affected field campaigns (Figure 4). These estimates demonstrate significantly greater drag compared to beneath smooth sea ice, where one would expect $C_d < 0.008$ [e.g., *Mellor et al.*, 1986; *Shirasawa and Ingram*, 1991]. The magnitude of these increases can be attributed to properties of the interface at each of the individual

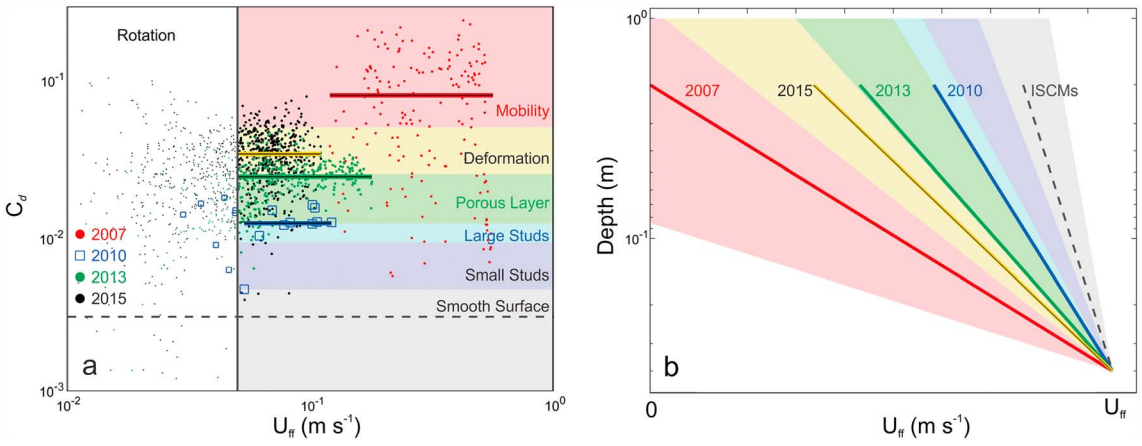

Figure 4. (a) Drag coefficient as a function of background flow speed from four field campaigns with mean estimates shown as solid lines. Background shading represents drag values published in nonpolar literature and described in the text (pale grey = smooth seabed/melting ice; grey/blue = gravel beach; pale blue = horse mussels/small frazil crystals; green = oyster bed/large platelet crystals; and yellow and red = deformation and mobility of a thick platelet layer). Values where $U_{ff} < 0.05\ m\ s^{-1}$ have been separated, as described in the text. The dashed line identifies the maximum C_d typically used to represent refreeze zones in Ice Shelf Cavity Models (ISCMs). (b) Modeled profiles of boundary layer speed, relative to far-field velocity, using typical C_d currently employed in ISCMs and mean C_d estimates from the field campaigns. Background shading represents the same interfacial conditions as for Figure 4a.

sites: the progressive crystal-derived disconnection between sea ice and ocean corresponds with a sequential increase in estimated drag coefficient:

1. In 2008, when no platelets or platelet layer were observed beneath the sea ice, the resulting boundary layer was too thin to allow estimation of C_d;
2. In 2010, the sea ice underside was studded with small platelets present in a very thin, and likely transient, layer and supported by limited supercooled water. The maximum observed C_d was $\cong 0.02$, with mean value $\overline{C_d} = 0.01 \pm 0.001$;
3. In 2013 and 2015, the platelets formed coherent and substantial layers >1 m thick, supported by significant volumes of supercooled water and attached to the base of the sea ice. Observed C_d was in the range 0.01–0.07 (2013: $\overline{C_d} = 0.02 \pm 0.002$; 2015: $\overline{C_d} = 0.03 \pm 0.003$);
4. In 2007, the platelets formed a thick (>1.5 m) lattice, which was subject to high flows and consequently was unattached and independently mobile beneath the sea ice. Velocity structure was affected to a depth of ~30 m (directly comparable with 2008 results), and C_d was estimated in the range 0.01–0.30 ($\overline{C_d} = 0.08 \pm 0.008$). The error estimate given here derives from the mean difference in C_d as estimated from 20 min and 60 min mean profiles, thereby incorporating aspects of both temporal variability and methodological uncertainty.

These observations comprise a range of possible ocean boundary layer responses to varying conditions of ocean temperature, flow speed, and platelet layer development. However, all imply roughness and drag significantly greater than has been previously described or is currently applied in numerical models of basal refreezing.

4. Discussion

The new observations demonstrate that the presence of crystals at the ice-ocean interface can have a substantial impact on boundary layer stress transfer and that this influence is ultimately determined by the degree of ice shelf influence. The evolution of drag coefficient seen here has a parallel in the nonpolar literature with the progression in boundary layer response to flow over a smooth, flat seabed to gravel beaches and shellfish beds.

Friedrichs and Wright [1997] examined the benthic boundary layer of a muddy seabed in a coastal embayment. Their background flow speeds were comparable to those observed here, ranging between 0.04 m s^{-1} and 0.14 m s^{-1}, and implying friction velocity, $u^* < 0.01$ m s^{-1}. They inferred C_d to lie in the range 0.001–0.006, with a mean value of 0.004, a range that mirrors the estimates derived from measurements beneath melting sea ice.

When studded with small individual ice crystals, as was observed 2010, the sea ice underside possesses roughness elements similar in height to that of a gravel beach. Correspondingly, *Thompson et al*. [2004] measured C_d in the range 0.003–0.01 for flow >0.1 m s^{-1} over a homogenous gravel bed. These estimates are similar to those for the thin and transient platelets observed by *McPhee et al*. [2016].

The overall morphology of an established platelet layer is comparable in size, shape, and spatial distribution to that of shellfish beds. *Green et al*. [1998] measured C_d in the range 0.008–0.012 over horse mussels, which are large shellfish with dimension of the order of 5–7 cm, spaced close together, and thus have much in common with the underside of ice coated in growing crystals.

In measurements that explicitly demonstrate the roughness attributable to shellfish-scale roughness, *Styles* [2014] examined two adjacent sandbanks, with and without oyster beds, but subject to identical background flows. Their estimate of $C_d = 0.004$ at the bare sandbank matches that for the typical seabed of *Friedrichs and Wright* [1997]. Conversely, their estimated drag coefficient over the oyster beds is around 0.025. This corresponds directly to the contrast between the roughness provided by a thick and porous layer of platelet ice (2013 and 2015) and that of melting sea ice.

These estimates describe elevated roughness from enhanced skin friction (size of individual crystals) and layer morphology. However, both effects are insufficient to explain the observed ocean boundary response in 2007. We therefore propose two further mechanisms by which the platelet layer may be able to extract energy from the upper ocean to further amplify the equivalent roughness. A third additional source of

enhanced roughness may stem from enhanced overall viscosity of ice crystals suspended in fluid flow, but this cannot be quantified with the present data.

4.1. Deformation

In their study of the hydrodynamics of submerged aquatic canopies, *Ghisalberti and Nepf* [2002, 2004] demonstrated deformation of the canopy in response to the passage of vortices at the interface. Known as the "monami," such coherent deformation is able to reduce stress internal to the canopy but can provide a further mechanism for extracting energy from the ocean boundary layer. Similarly, the open, porous structure created as crystals grow through one another may deform or collapse in response to external stress.

Ghisalberti and Nepf [2002, 2004] found that a region of strong shear exists at the interface between the canopy and ambient water, owing to the inflection in velocity structure and drag discontinuity there. Thus, the top of the canopy is characterized as a region of rapid exchange with a strong influence on vertical transport. Similarly, the boundary layer immediately beneath the platelet layer would be a region of rapid vertical exchange, where the platelet layer is able to deform in response to external stress in an analogous manner.

4.2. Mobility

A final mechanism we consider here is the mobility of the platelet layer as a coherent whole. Despite the buoyancy of the platelet ice crystals, a fluid-filled gap was observed between the platelet layer and the stationary sea ice in 2007. This allowed the platelet layer freedom of lateral movement in response to frictional drag exerted by the ocean beneath, contributing to a greater net transfer of momentum at the ice-ocean interface. We expect that, during periods of low flow, the gap would not be maintained due to the positive buoyancy of the platelet layer, allowing the platelet layer to come into direct contact with the sea ice, thereby introducing an additional frictional force. This differentiated response is implied in the velocity profile structures of peak and transitional tidal flows (Figure 3b or 3c).

Shen and Wang [1995] observed "ice jams" in the Hequ region of the Yellow River that bear significant resemblance to the platelet layer observed here. They reported frazil granules with a mean diameter of 1 cm and ice jam solid volume fraction of 0.6 (porosity = 0.4), which are both of similar order to observations in the present study. Treating the jam in a similar manner to a seafloor sediment bedload, they modeled the boundary layer response taking into account crystal rise velocity and deposition via the Rouse number, $z = \omega/\kappa u^*$, where ω is the rise/fall velocity, κ is von Karman's constant, and u^* is the shear velocity. The velocity profile thus predicted beneath a fully mobile ice jam is logarithmic with distance from the base of the jam [*Shen and Wang*, 1995]. That this prediction is made from fresh water flow, for which stratification can be eliminated as a determining factor, serves to identify the structure of the platelet layer as the causal agent that determines the velocity structure in the boundary layer.

5. Conclusions

This study presents estimates of drag coefficients from four sites within a major outflow of ice shelf water (ISW) from the Ross/McMurdo Ice Shelf ocean cavity. The ISW was supercooled through pressure relief during its approach McMurdo Sound, leading to deposition of thick layers of ice crystal trapped by buoyancy at the ice-ocean interface. By working where the ice cover is relatively thin (i.e., the sea ice immediately adjacent to the front of the ice shelf), and hence where the ocean boundary layer is relatively accessible, we have been able to observe crystal-affected ice-ocean interactions in a variety of environmental conditions.

Three different velocity acquisition techniques yielded comparable estimates of drag coefficient by appealing to the law of the wall model of boundary layer behavior. From these we conclude that even small and transient crystals at the ice-ocean interface significantly increase stress transfer at the boundary through enhanced skin friction. The effect is amplified, by orders of magnitude, where the crystals have developed into thick layers that may also be subject to flows fast enough to disassociate them from the overlying ice. This prompts our suggestion that four modes of effective drag—skin friction, form drag, deformation, and mobility—may be operating synchronously. Quantification of a fifth potential contribution—the effect of enhanced viscosity of ice crystals suspended in fluid flow—was beyond the scope of this study.

These new observations suggest that drag coefficients used in numerical models of sea ice affected by ice shelf cavities should be revised upward substantially, dependent on the degree and persistence of

supercooling. This, in turn, will affect how these models simulate the fate of cavity-sourced plumes and in doing so will influence predictions of sea ice growth and stratification around Antarctica [see *Langhorne et al*., 2015].

The process of pressure-induced supercooling and subsequent buoyant deposition of ice crystals is replicated beneath all of the major cold cavity ice shelves. Marine ice is thought to buffer interactions between ice shelf and ocean [*Eicken and Lange*, 1989], and to provide a stabilizing influence on ice shelves by healing rifts [*Khazendar and Jenkins*, 2003], smoothing basal regions that could be expected to be heavily crevassed [*Smedsrud and Jenkins*, 2004], and allowing ice shelves to deform rather than fail in response to stress [*Holland et al*., 2009]. Marine ice makes up significant volumes of the Filchner [*Grosfeld et al*., 1998], Ronne [*Engelhardt and Determann*, 1987], Amery [*Craven et al*., 2005, 2009; *Fricker et al*., 2001], Ross [*Neal*, 1979; *Rignot et al*., 2013], McMurdo [*McCrae*, 1984], and Larsen C Ice Shelves [*Holland et al*., 2009] and could be expected to exert similar or greater drag on the ocean boundary layer to that observed in this study.

In accordance with the evolution of this topic in the nonpolar literature, the use of drag coefficients derived beneath smooth, melting Arctic sea ice should no longer be considered appropriate in numerical prediction of Antarctic sea ice and ice shelf evolution. This should motivate spatially differentiated treatment of boundary interaction beneath ice shelves, determined by whether the ice shelf is locally melting or refreezing [*Gwyther et al*., 2015] which, in conjunction with improved basal topography, will improve understanding of sub-ice shelf circulation and processes

The net effect of incorporating enhanced roughness will depend on the stratification it interacts with, as this will determine the rate at which heat is entrained from below and thereby made available for turbulent exchange with the interface. At a minimum, a differentiated numerical approach to zones of melt and freeze is required. More sophisticated parameterizations, taking into account local conditions of flow, pressure, and temperature, would also be appropriate, although these relationships are yet to be quantified.

Acknowledgments

Tim Haskell, Brett Grant, Cecilia Bitz, Gabby O'Connor, Andy Mahoney, Alex Gough, Brian Staite, and Antarctica New Zealand are thanked for their assistance in the field. Inga Smith, Pat Langhorne, Mike Williams, Ken Hughes, Greg Leonard, Ben Galton-Fenzi, and David Gwyther are thanked for valuable discussion. David Plew is thanked for the loan of equipment. We thank two anonymous reviewers for their insightful comments which have helped to improve the clarity and applicability of the manuscript. Funding was provided by the Royal Society of New Zealand Marsden Fund, NIWA Core Funding, Antarctica New Zealand, a University of Otago Research Grant, the Deep South National Science Challenge project "Targeted observations and process-informed modeling of Antarctic sea ice," and the New Zealand Antarctic Research Institute. Metadata are lodged with Antarctica New Zealand. Data are archived with NIWA, New Zealand, and are available from the authors upon request (natalie.robinson@niwa.co.nz).

References

Craven, M., F. Carsey, A. Behar, J. Matthews, R. Brand, A. Elcheikh, S. Hall, and A. Treverrow (2005), Borehole imagery of meteoric and marine ice layers in the Amery Ice Shelf, East Antarctica, *J. Glaciol.*, *51*(172), 75–84.

Craven, M., I. Allison, H. A. Fricker, and A. R. Warner (2009), Properties of a marine ice layer under the Amery Ice Shelf, East Antarctica, *J. Glaciol.*, *55*(192), 717–728, doi:10.3189/002214309789470941.

Eicken, H., and M. A. Lange (1989), Development and properties of sea ice in the coastal regime of the southeastern Weddell Sea, *J. Geophys. Res.*, *94*, 8193–8206, doi:10.1029/JC094iC06p08193.

Engelhardt, H., and J. Determann (1987), Borehole evidence for a thick layer of basal ice in the central Ronne Ice Shelf, *Nature*, *327*, 318–319.

Fricker, H. A., S. Popov, I. Allison, and N. Young (2001), Distribution of marine ice beneath the Amery Ice Shelf, *Geophys. Res. Lett.*, *28*, 2241–2244, doi:10.1029/2000GL012461.

Friedrichs, C. T., and L. D. Wright (1997), Sensitivity of bottom stress and bottom roughness estimates to density stratification, Erckernfjorde Bay, southern Baltic Sea, *J. Geophys. Res.*, *102*, 5721–5732, doi:10.1029/96JC03550.

Ghisalberti, M., and H. M. Nepf (2002), Mixing layers and coherent structures in vegetated aquatic flows, *J. Geophys. Res. 107*(C2), 3011, 10.1029/2001JC000871.

Ghisalberti, M., and H. M. Nepf (2004), The limited growth of vegetated shear layers, *Water Resour. Res.*, *40*, W07502, doi:10.1029/2003WR002776.

Green, M. O., J. E. Hewitt, and S. F. Thrush (1998), Seabed drag coefficient over natural beds of horse mussels (*Atrina zelandica*), *J. Mar. Res.*, *56*(3), 613–637.

Grosfeld, K., H. H. Hellmer, M. Jonas, H. Sandhger, M. Schulte, and D. G. Vaughan (1998), Marine ice beneath Filchner Ice Shelf: Evidence from a multi-disciplinary approach, in *Ocean, Ice and Atmosphere: Interactions at the Antarctic Continental Margin*, *Antarctic Res. Ser.*, vol. 75, edited by S. Jacobs and R. Weiss, pp. 319–339, AGU, Washington, D. C.

Gwyther, D. E., B. K. Galton-Fenzi, M. S. Dinniman, J. L. Roberts, and J. R. Hunter (2015), An investigation of the impact of basal roughness on melting and freezing in ice shelf-ocean models, *Ocean Model.*, *95*, 38–52.

Holland, P. R., H. F. J. Corr, D. G. Vaughan, A. Jenkins, and P. Skvarca (2009), Marine ice in Larsen Ice Shelf, *Geophys. Res. Lett.*, *36*, L11604, doi:10.1029/2009GL038162.

Hughes, K. G., P. J. Langhorne, G. H. Leonard, and C. L. Stevens (2014), Extension of an Ice Shelf Water plume model beneath sea ice with application in McMurdo Sound, Antarctica, *J. Geophys. Res. Oceans*, *119*, 8662–8687, doi:10.1002/2013JC009411.

Hunkeler, P., S. Hendricks, M. Hoppmann, S. Paul, and R. Gerdes (2015), Towards an estimation of sub-sea-ice platelet-layer volume with multi-frequency electromagnetic induction sounding, *Ann. Glaciol.*, *56*(69), 137–146, doi:10.3189/2015AoG69A705.

Jenkins, A., K. W. Nicholls, and H. F. J. Corr (2010), Observation and parameterisation of ablation at the base of Ronne Ice Shelf, Antarctica, *J. Phys. Oceanogr.*, *40*(10), 2298–2312.

Khazendar, A., and A. Jenkins (2003), A model of marine ice formation within Antarctic ice shelf rifts, *J. Geophys. Res.*, *108*(C7), 3235, doi:10.1029/2002JC001673.

Langhorne, P. J., et al. (2015), Ice shelf-ocean heat flux: Spatial and temporal distribution of platelet ice around coastal Antarctica, *Geophys. Res. Lett.*, *42*, 5442–5451, doi:10.1002/2015GL064508.

Mahoney, A. R., A. J. Gough, P. J. Langhorne, N. J. Robinson, C. L. Stevens, M. J. M. Williams, and T. G. Haskell (2011), The seasonal appearance of ice shelf water in coastal Antarctica and its effect on sea ice growth, *J. Geophys. Res.*, *116*, C11032, doi:10.1029/2011JC007060.

McCrae, I. R. (1984), A summary of glaciological measurements made between 1960 and 1984 on the McMurdo Ice Shelf, Antarctica, Tech. Rep. 360, School of Eng., Dep. of Theoretical and Appl. Mechanics, Univ. of Auckland, Auckland, New Zealand.
McPhee, M. G. (2008), *Air-Ice-Ocean-Interaction: Turbulent Ocean Boundary Layer Exchange Processes*, pp. 215, Springer, New York.
McPhee, M. G., C. L. Stevens, I. J. Smith, and N. J. Robinson (2016), Turbulent heat transfer as a control of platelet ice growth in supercooled under-ice ocean boundary layers, *Ocean Sci.*, *12*, 507–515, doi:10.5194/osd-12-2807-2015.
Mellor, G. L., M. G. McPhee, and M. Steele (1986), Ice-seawater turbulent boundary layer interaction with melting or freezing, *J. Phys. Oceanogr.*, *16*(11), 1829–1846.
Neal, C. S. (1979), The dynamics of the Ross Ice Shelf revealed by radio echo-sounding, *J. Glaciol.*, *24*(90), 295–307.
Rignot, E., S. Jacobs, J. Mouginot, and B. Scheuchl (2013), Ice-shelf melting around Antarctica, *Science*, *341*, 266–270.
Robinson, N. J., M. J. M. Williams, C. L. Stevens, P. J. Langhorne, and T. G. Haskell (2014), Evolution of a supercooled ISW plume with an actively-growing matrix of platelet ice, *J. Geophys. Res. Oceans*, *119*, 3425–3446, doi:10.1002/2013JC009399.
Shen, H. T., and D. S. Wang (1995), Under cover transport and accumulation of frazil granules, *J. Hydraulic Eng.*, *121*(2), 184–195.
Shirasawa, K., and R. G. Ingram (1991), Characteristics of the turbulent oceanic boundary layer under sea ice. Part 2: Measurements in southeast Hudson Bay, *J. Mar. Syst.*, *2*(1), 161–169.
Smedsrud, L. H., and A. Jenkins (2004), Frazil ice formation in an ice shelf water plume, *J. Geophys. Res.*, *109*, C03025, doi:10.1029/2003JC001851.
Smith, I. J., P. J. Langhorne, T. G. Haskell, H. J. Trodahl, R. Frew, and M. R. Vennell (2001), Platelet ice and the land-fast ice of McMurdo Sound, Antarctica, *Ann. Glaciol.*, *33*, 21–27.
Styles, R. (2014), Flow and turbulence over an oyster reef, *J. Coastal Res.*, *31*(4), 978–985.
Thompson, C. E. L., C. L. Amos, M. Lecouturier, and T. E. R. Jones (2004), Flow deceleration as a method of determining drag coefficient over roughened flat beds, *J. Geophys. Res.*, *109*, C03001, doi:10.1029/2001JC001262.